Journal of Materials Chemistry B

ROYAL SOCIETY OF CHEMISTRY

COMMUNICATION

View Article Online
View Journal | View Issue

Cite this: J. Mater. Chem. B, 2025, 13, 9043

Received 16th April 2025,
Accepted 30th June 2025

DOI: 10.1039/d5tb00892a

rsc.li/materials-b

Near infrared light driven nanocatalyst with hole-mediated GSH-depletion for augmented memory therapy†

Zhiming Deng,[ab] Jialian Li,[b] Chunqian Hu,*[e] Yiyu Tang,[d] Jun Zhong,[f] Hanlin Wei,*[b] Jiayou Tao*[a] and Qi Zheng*[c]

Photocatalytic therapy holds promise as a non-invasive approach for tumor treatment and is currently under active development. However, its effectiveness relies on continuous laser radiation, which can limit its practical application. To overcome this challenge, we designed a novel composite photocatalyst composed of SnO_2 nanoparticles strategically decorated on Cu_2O nanospheres. This unique design creates a p–n heterojunction that serves as a robust driving force for photogenerated electrons and holes under 808 nm laser illumination. This enhanced photocatalytic activity results in the generation of reactive oxygen species (ROS) and depletion of glutathione (GSH), further augmenting the anti-tumor effect. It is noteworthy that the Cu_2O@SnO_2 nanocatalyst exhibits remarkable "memory" of photocatalytic activity, ensuring effective tumor treatment even after the laser is stopped. This study offers a promising approach for sustained tumor treatment, even after the laser radiation has been stopped.

Various organic and inorganic nanocatalysts have been extensively studied for applications in solar energy conversion, environmental applications, antibacterial treatments, and anti-tumor treatments.[1–8] It is generally recognized that photocatalysts have the ability to generate reactive oxygen species (ROS) through light illumination, subsequently utilizing these species to oxidize and reduce diverse substances. Nevertheless, the generation of ROS heavily depends on persistent illumination, thereby limiting the functionality of numerous nanocatalysts to operate exclusively upon exposure to light.[9–15] This becomes particularly crucial in anti-tumor therapy, where the continuous release of ROS is essential for effective treatment. Therefore, investigating a novel nanocatalyst with photocatalytic memory would be highly advantageous.[16,17] Such a catalyst has the potential to store a part of its photoactivity during light exposure, maintaining its activity even when the light source is removed, thereby enabling continuous and efficient tumor therapy through photocatalytic memory.

Currently, the majority of traditional nanocatalysts developed are activated by ultraviolet-visible (UV-vis) light, resulting in limited penetration depth and subsequently compromising the effectiveness of deep-tissue anti-tumor therapy. Conversely, near-infrared (NIR) light has attracted significant attention due to its superior ability to penetrate deeper tissues, offering greater potential for effective anti-tumor therapy.[18–23] Therefore, research efforts have been focused on developing lanthanide-based nanocatalysts that can be activated by NIR light, in combination with lanthanide upconversion (UC) nanoparticles and photocatalytic semiconductors, in an attempt to enhance the efficacy of anti-tumor therapy.[24–26] These nanocatalysts utilize UC luminescence to convert the absorbed NIR light into UV-vis light. However, the low conversion efficiency of these nano-converters remains a significant challenge in improving the efficiency of photocatalytic therapy. Therefore, there is an urgent need to develop a novel type of NIR-light-activated nanocatalyst with photocatalytic memory, in an attempt to effectively treat deep-tissue malignant tumors.

The tumor microenvironment (TME) usually presents over-expressed endogenous glutathione (GSH),[27,28] which is a general anti-oxidant to scavenge ROS. The effectiveness of ROS-dependent photocatalytic therapy for tumors will be significantly limited if endogenous GSH cannot be effectively depleted in a timely

[a] Key Laboratory of Hunan Province on Information Photonics and Freespace Optical Communications, School of physics and electrical sciences, Hunan Institute of Science and Technology, Yueyang, 414006, People's Republic of China. E-mail: taojy2572@163.com
[b] State Key Laboratory for Chemo/Bio-Sensing and Chemometrics, College of Chemistry and Chemical Engineering, Hunan University, Changsha 410082, China. E-mail: hlwei@hnu.edu.cn
[c] Key Laboratory for Micro-Nano Optoelectronic Devices of Ministry of Education, School of Physics and Electronics, Hunan University, Changsha, China. E-mail: zhengqi@hnu.edu.cn
[d] Hunan Provincial Maternal and Child Health care Hospital, China
[e] Department of Clinical Laboratory, Yueyang Central Hospital of Hunan Province, 414000, China. E-mail: 15580128585@163.com
[f] College of Medical Engineering and Technology, Hunan Institute of Engineering, Xiangtan 411105, China

† Electronic supplementary information (ESI) available. See DOI: https://doi.org/10.1039/d5tb00892a

manner. Therefore, GSH depletion is crucial for the efficient treatment of tumors using ROS-based photocatalytic therapy. Fortunately, nanocatalysts generate electrons and holes upon exposure to light, which possess both reductive and oxidative capabilities. Notably, electrons with high reductive potential can be harnessed to generate ROS. Additionally, holes with enough high oxidative capability[29] can be utilized to deplete GSH to regulate the TME. Therefore, the development of a nanocatalyst possessing suitable potential for GSH depletion and ROS production is vital for anti-tumor therapy and remains a challenge.

Herein, a novel 808 nm laser-triggered $Cu_2O@SnO_2$ nanocatalyst was developed for hole/ROS photocatalytic memory therapy. Our designed $Cu_2O@SnO_2$ nanocatalyst presents enhanced production and separation of electron–hole pairs, enabling on-demand ROS/holes therapy under 808 nm laser irradiation. Interestingly, the designed nanocatalyst can break the redox balance and modulate the TME *via* the depletion of the endogenous GSH. More importantly, the designed nanocatalyst exhibits photocatalytic memory capability for anti-tumor therapy, which can further improve the treatment efficiency for malignant tumors.

Results and discussion

The photocatalytic memory ability of $Cu_2O@SnO_2$ composite material can be attributed to its p–n heterostructure, which facilitates efficient electron transfer. Additionally, the SnO_2 possesses the ability to store and release electrons, enabling the material to maintain its photocatalytic activity even under dark conditions.[30] This characteristic makes $Cu_2O@SnO_2$ potentially valuable in tumor treatment. To achieve a nanocatalyst with highly efficient ROS/holes memory therapy, an 808 nm laser driven $Cu_2O@SnO_2$ nanocatalyst was designed by coating SnO_2 on the surface of a Cu_2O nanosphere (Scheme 1). As shown in Fig. 1A–C, the SnO_2 nanoparticles were successfully deposited on the surface of the Cu_2O nanosphere to generate a core–satellite-based heterojunction. The mean size of Cu_2O was ~192 nm, while that of $Cu_2O@SnO_2$ was ~202 nm (Fig. 1D). Furthermore, the coexistence of Sn, Cu, and O elements was observed in the energy dispersive X-ray (EDX) spectrum of the $Cu_2O@SnO_2$ nanocatalyst (Fig. 1E and F), illustrating the successful deposition of SnO_2 nanoparticles on the surface of the Cu_2O nanosphere. X-ray diffraction (XRD) was used to evaluate the process of formation of the $Cu_2O@SnO_2$ nanocatalyst (Fig. 1G), clearly showing that the samples changed from a high-purity Cu_2O nanosphere (JCPDS: 05-0667) to a $Cu_2O@SnO_2$ nanocatalyst. SnO_2 was then decorated electrostatically onto the surface of Cu_2O (Fig. 1H), as confirmed by the change in zeta potential (from −0.5 to +20 mV). Furthermore, the elemental composition of the $Cu_2O@SnO_2$ nanocatalyst was investigated by X-ray photoelectron spectroscopy (XPS). The

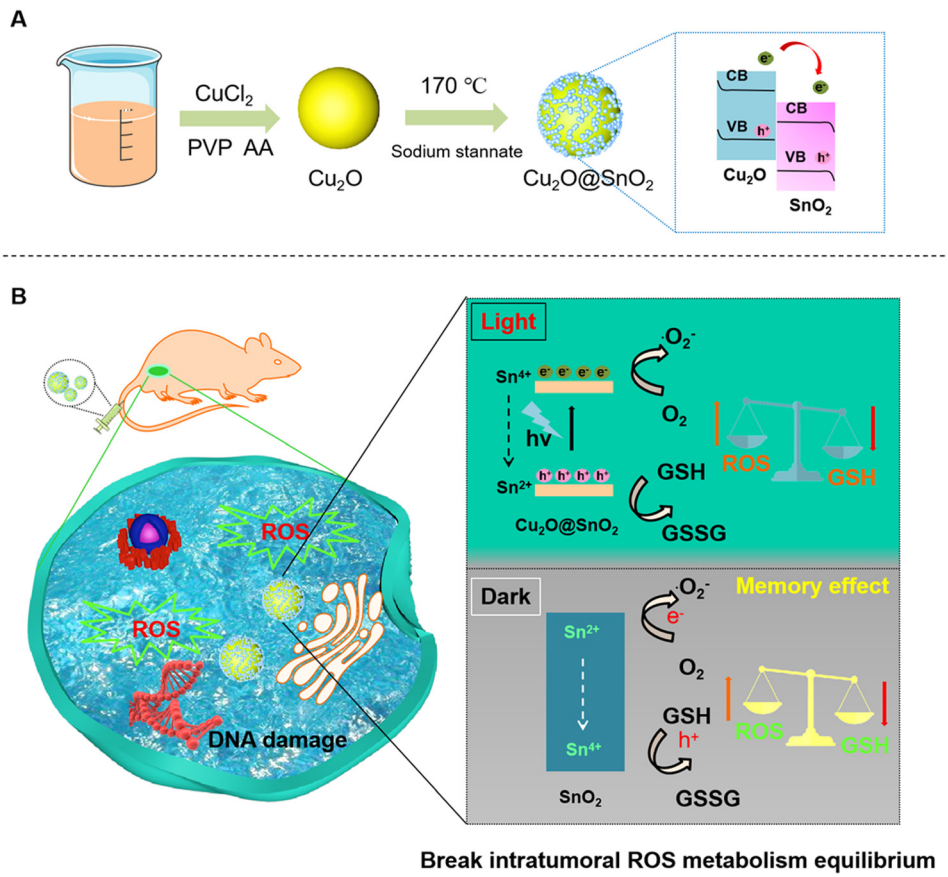

Scheme 1 Schematic illustration of the 808 nm laser driven $Cu_2O@SnO_2$ nanocatalyst with electron-triggered ROS generation and hole-mediated GSH depletion for synergistic anti-tumor memory therapy.

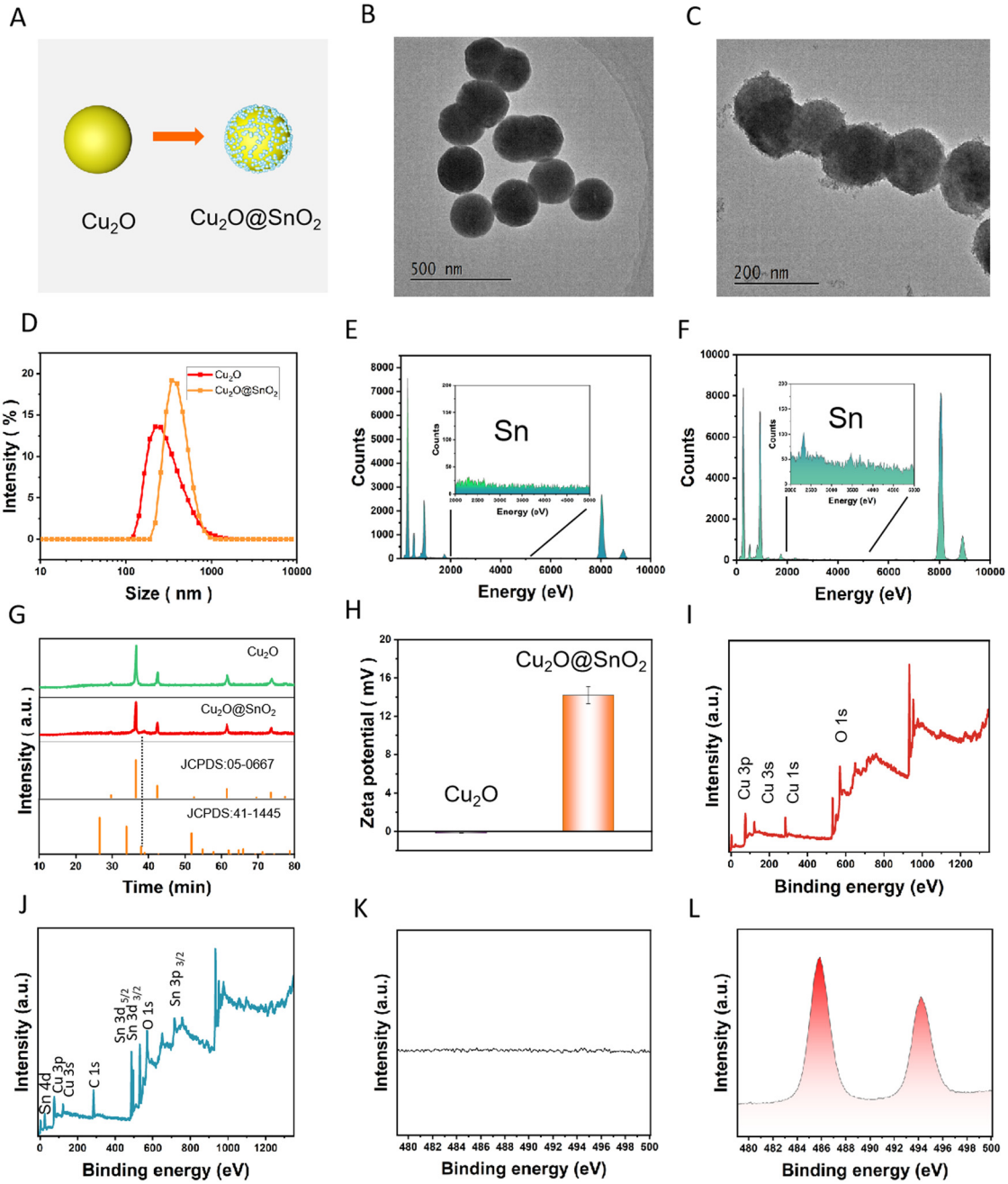

Fig. 1 Structure of the $Cu_2O@SnO_2$ nanocatalyst. (A) Schematic illustration of the formation of the $Cu_2O@SnO_2$ nanocatalyst. (B) and (C) TEM images of the Cu_2O nanosphere and $Cu_2O@SnO_2$ nanocatalyst, respectively. (D) Hydrodynamic size of Cu_2O and $Cu_2O@SnO_2$ nanocatalyst. (E) and (F) The EDX spectra of Cu_2O and $Cu_2O@SnO_2$ nanocatalyst. (G) XRD patterns of Cu_2O and $Cu_2O@SnO_2$ nanocatalyst. (H) Zeta potential analysis of Cu_2O and $Cu_2O@SnO_2$ nanocatalyst. (I) and (J) XPS of the synthesized Cu_2O and $Cu_2O@SnO_2$ nanocatalyst. (K) XPS peaks of Sn of Cu_2O. (L) The XPS peaks of Sn of $Cu_2O@SnO_2$ nanocatalyst.

$Cu_2O@SnO_2$ nanocatalyst was composed mainly of Sn, Cu, and O elements (Fig. 1K and L). As shown in Fig. S1 (ESI†), the absorption spectra of the $Cu_2O@SnO_2$ nanocatalyst in water, PBS and DMEM did not significantly change over 40 h, indicating the structural integrity and stability of the nanocatalyst.

Under 808 nm laser irradiation, the $Cu_2O@SnO_2$ nanocatalyst with the photocatalytic "memory" effect can promote the separation of electrons and holes, leading to efficient generation of ROS and endogenous GSH depletion. As shown in Fig. 2A, the $Cu_2O@SnO_2$ nanocatalyst shows obvious absorption at 808 nm, making it an ideal nanomaterial for photocatalytic application in NIR regions. To investigate the mechanism of photocatalysis, the band gap of our designed nanocatalyst was studied. The band gap of the $Cu_2O@SnO_2$ nanocatalyst was about 1.75 eV (Fig. 2B). VB-XPS spectroscopy was used to determine the potentials of VB in the Cu_2O

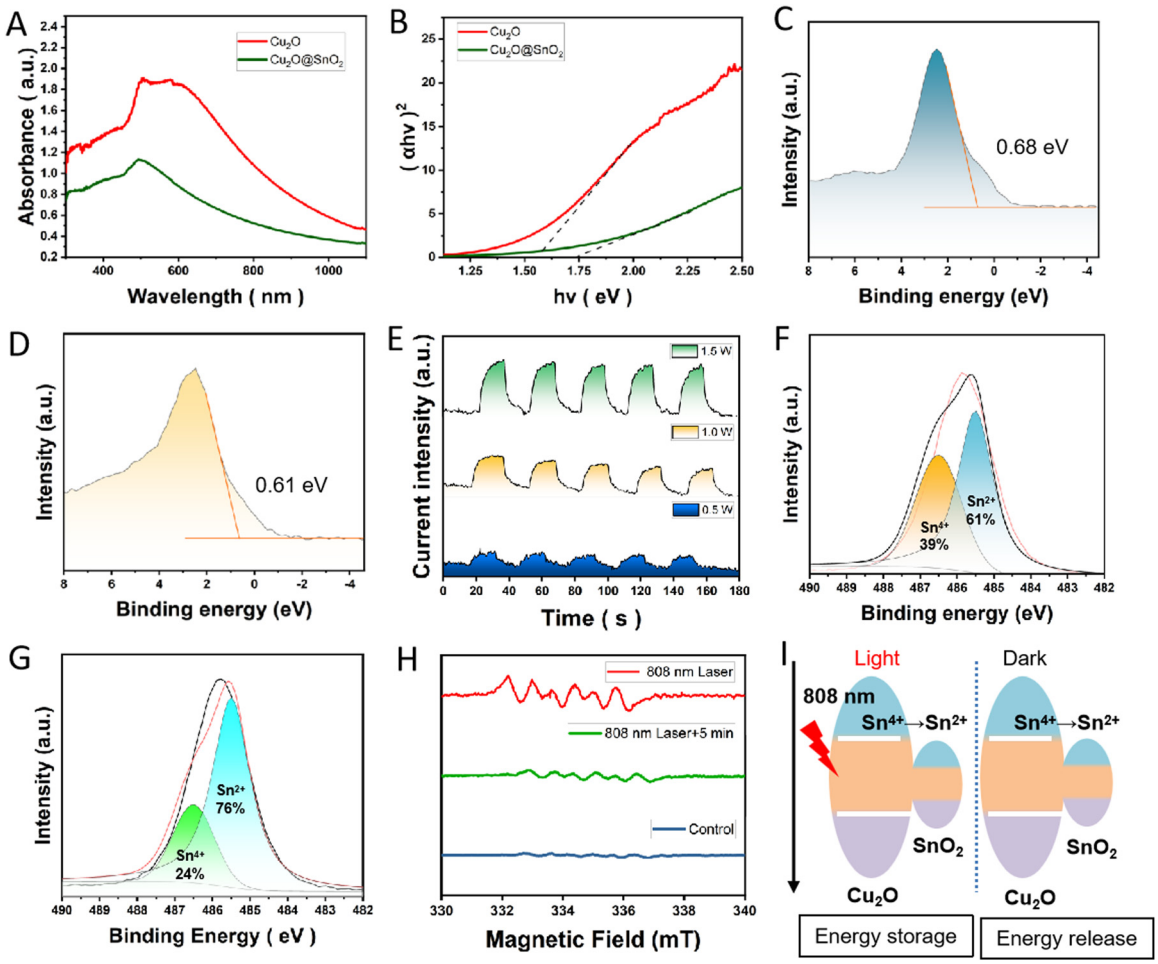

Fig. 2 The memory photocatalysis mechanism of the $Cu_2O@SnO_2$ nanocatalyst. (A) The UV-vis spectra of the Cu_2O nanosphere and $Cu_2O@SnO_2$ nanocatalyst. (B) Plot of $(\alpha h\nu)^2$ *versus* photon energy ($h\nu$) of the Cu_2O nanosphere and $Cu_2O@SnO_2$ nanocatalyst. (C) and (D) VB-XPS spectra of Cu_2O and $Cu_2O@SnO_2$ nanocatalyst. (E) The photocurrent curves of the $Cu_2O@SnO_2$ nanocatalyst under 808 nm laser radiation with different power densities. (F) and (G) XPS analysis of $Cu_2O@SnO_2$ before and after 808 laser irradiation. (H) The ESR spectra of the $Cu_2O@SnO_2$ nanocatalyst under 808 nm laser irradiation. (I) Mechanistic diagram of photocatalytic memory therapy.

nanosphere and $Cu_2O@SnO_2$ nanocatalyst. The VB values *vs.* NHE were calculated to be 0.44 eV and 0.37 eV for the Cu_2O nanosphere and $Cu_2O@SnO_2$ nanocatalyst, respectively. The CB position can be determined from $E_{CB} = E_{VB} - E_g$, and E_{CB} was calculated to be −1.38 eV for the $Cu_2O@SnO_2$ nanocatalyst (Fig. 2C and D). Thus, the CB potential of the $Cu_2O@SnO_2$ nanocatalyst is more negative than the redox potential of $O_2/{}^{\bullet}O^{2-}$ (−0.046 V *vs.* NHE, pH = 0), which can generate ${}^{\bullet}O_2^-$ ROS. Meanwhile, the VB potential of the $Cu_2O@SnO_2$ nanocatalyst is relatively higher than the oxidative potential of GSH to GSSG (≥0.32 eV), leading to efficient GSH depletion.

We first evaluated the photocurrent generated from the $Cu_2O@SnO_2$ nanocatalyst under 808 nm laser irradiation. As indicated in Fig. 2E, an obvious photocurrent was achieved in the $Cu_2O@SnO_2$ nanocatalyst upon irradiation by an 808 nm laser, confirming efficient electron–hole separation. The photocurrent of the $Cu_2O@SnO_2$ nanocatalyst increased with increasing laser power. Thus, the $Cu_2O@SnO_2$ nanocatalyst featuring excellent conductivity is expected to promote more ROS production by facilitating the separation of electron–hole pairs and impeding their re-combination during 808 nm laser-triggered photocatalysis. Fig. 2F shows the high-resolution XPS scan over Sn_{3d} peaks under 808 nm laser illumination. The Sn^{4+}/Sn^{2+} ratio was determined to be ∼24 : 76. Compared to that without illumination, as shown in Fig. 2G, a large proportion of Sn^{4+} was reduced to Sn^{2+}, which came from the transfer of photogenerated electrons from Cu_2O to SnO_2 under 808 nm laser illumination and the subsequent trapping of some of these electrons by SnO_2. Then, electron spin resonance (ESR) was employed. As shown in Fig. 2H, the ESR spectrum demonstrated an obvious 1 : 1 : 1 : 1 : 1 : 1 sextuplet signal, further elucidating the generation of ${}^{\bullet}O_2^-$ under 808 nm laser irradiation. Measurement conducted in the dark on the $Cu_2O@SnO_2$ nanocatalyst before exposure also demonstrated ${}^{\bullet}O_2^-$ signals. Our spin-trapping EPR measurements suggest that the "memory" effect resulted from the production of reactive radicals when the 808 nm laser was shut off. As these radicals rapidly react with biomolecules, what determines the duration of the

"memory" effect is the rate of charge release from Sn^{2+} particles. Fig. 2I shows the proposed energy band structure of the $Cu_2O@SnO_2$ p–n heterojunction, the photocatalytic activity enhancement mechanism under 808 nm laser illumination and the post-illumination photocatalytic "memory" mechanism in the dark. When p-type Cu_2O and n-type SnO_2 form a heterostructure, there is a concentration gradient of charge carriers at the interface. Therefore, electrons diffuse from SnO_2 to Cu_2O, and holes diffuse in the opposite direction until an equilibrium state is reached, forming an internal electric field at the interface. Under 808 nm laser irradiation, only Cu_2O is excited to produce electron–hole pairs. The combination of a large conduction band potential difference and the internal electric field provides a strong driving force for the transfer of photogenerated electrons from the conduction band of Cu_2O to SnO_2, which is confirmed by XPS experimental evidence, such as the production of ROS and the change in Sn chemical state from Sn^{4+} to Sn^{2+}. When 808 nm laser irradiation is stopped, trapped electrons can be released from SnO_2, and due to the matching reduction potentials of these released electrons and oxygen, electron reduction reactions can occur to produce ROS. At the same time, the vacancies can achieve the degradation of GSH. Therefore, after the laser is turned off, $Cu_2O@SnO_2$ can demonstrate post-illumination photocatalytic "memory" to produce ROS and GSH degradation in the dark.

Next, we detected the GSH depletion ability of the $Cu_2O@SnO_2$ nanocatalyst by 5,5′-dithiobis(2-nitrobenzoic acid) (DTNB).[31] With increasing 808 nm laser irradiation time, the GSH level decreased sharply (Fig. 3A–C) in the presence of the $Cu_2O@SnO_2$ nanocatalyst. The depletion of GSH by the $Cu_2O@SnO_2$ nanocatalyst can maintain a highly efficient ROS level in the TME by breaking the redox balance in the tumor. To evaluate the properties of ROS generation under 808 nm laser irradiation, 1,3-diphenylisobenzofuran (DPBF) was utilized to indicate the ability for ROS production. The absorbance intensity of the DPBF peak in the $Cu_2O@SnO_2$ nanocatalyst

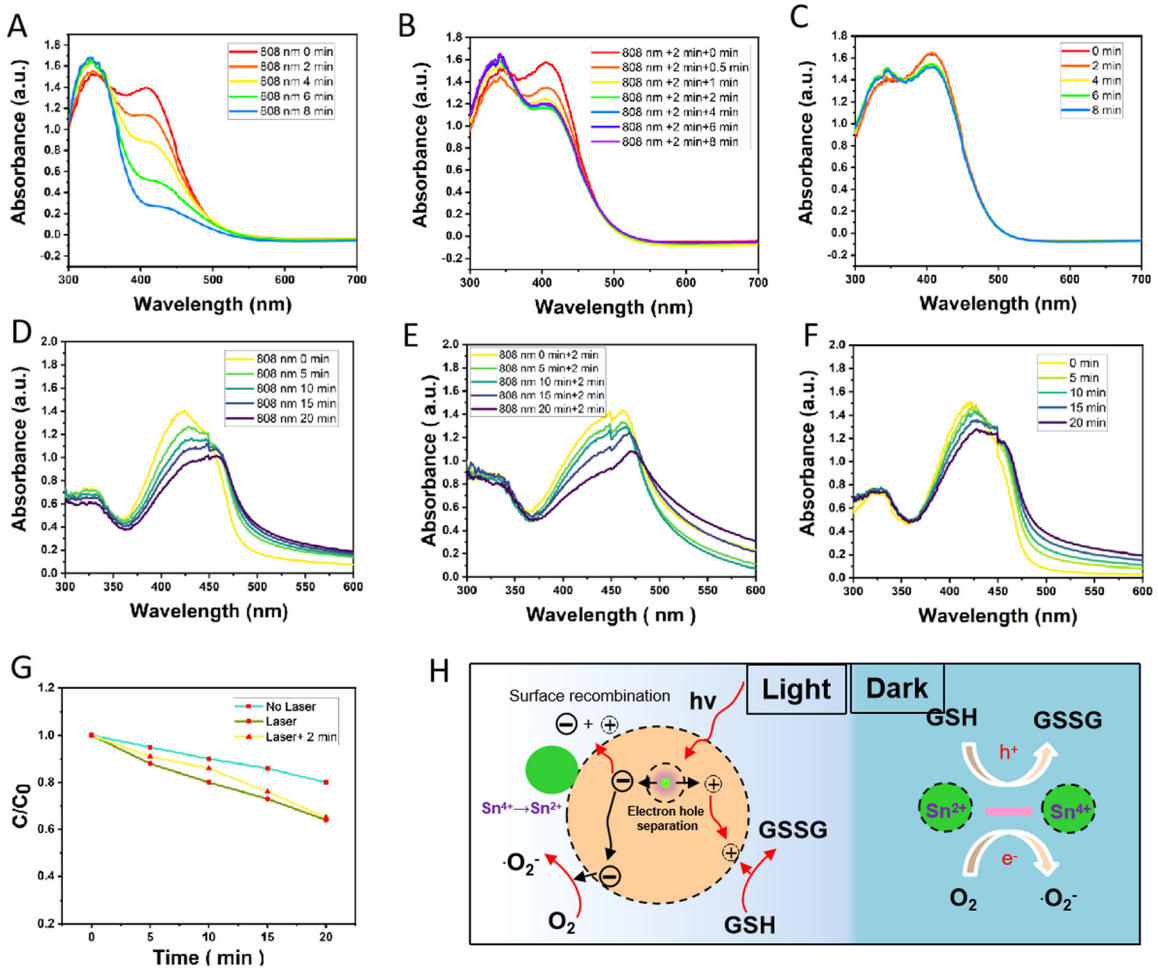

Fig. 3 ROS generation and GSH depletion assay. (A) GSH depletion by the $Cu_2O@SnO_2$ nanocatalyst after 808 nm laser irradiation. (B) Degradation of GSH by the $Cu_2O@SnO_2$ nanocatalyst after 2 minutes of laser irradiation. (C) GSH depletion by the $Cu_2O@SnO_2$ nanocatalyst in the presence of hole scavenger EDTA-2Na after 808 nm laser irradiation. (D) and (E) Time-dependent UV-visible absorption spectra of DPBF after 0 and 2 min of 808 nm laser irradiation on the $Cu_2O@SnO_2$ nanocatalyst. (F) Time-dependent UV-vis absorbance spectra of DPBF after 808 nm laser irradiation. (G) The normalized absorption intensity at 410 nm of DPBF under 808 nm and without 808 nm laser irradiation. (H) Schematic diagram of ROS production and GSH degradation in photocatalytic memory therapy.

decreased as the irradiation time of the 808 nm laser was prolonged (Fig. 3D, E, and F, G), indicating the efficient generation of ROS. Therefore, our designed 808 nm laser activated $Cu_2O@SnO_2$ nanocatalyst with efficient separation of electrons and holes showed excellent GSH depletion and ROS generation, which could be used as ideal nanocatalyst for *in vivo* anti-tumor therapy. It should be noted that the $Cu_2O@SnO_2$ nanocatalyst continued to produce ROS for up to 2 min after the 808 nm laser irradiation was stopped. This is mainly due to the energy released from the transformation of Sn^{2+} into Sn^{4+} (Fig. 3H).

Next, we conducted a thorough assessment of the cytotoxicity of the $Cu_2O@SnO_2$ nanocatalyst in 4T1 cancer cells using a Cell Counting Kit-8 (CCK-8) assay. Our findings revealed that the $Cu_2O@SnO_2$ nanocatalyst exhibited excellent biocompatibility (Fig. S2, ESI†). Next, we embarked on a detailed investigation of its effects on intracellular ROS generation within 4T1 cancer cells. To gain insights into the ROS-generating capacity of various treatments, we conducted a series of experiments using PBS, $Cu_2O@SnO_2$ nanocatalyst and $Cu_2O@SnO_2$ nanocatalyst + 808 nm laser in 4T1 cells. By capturing confocal images of cancer cells stained with DCHF-DA (Fig. S3, ESI†), we observed a significant difference: cells treated with the $Cu_2O@SnO_2$ nanocatalyst combined with an 808 nm laser exhibited strong green fluorescence, whereas cells treated with the $Cu_2O@SnO_2$ nanocatalyst alone or PBS demonstrated negligible fluorescence. This clear demonstration underscores that the $Cu_2O@SnO_2$ nanocatalyst + 808 nm laser is capable of generating significant ROS within cancer cells.

To comprehensively evaluate biocompatibility, we provide the histopathology results of major organs, blood biochemical parameters, and blood routine examination results. As shown in Fig. S4 (ESI†), through H&E staining, no obvious pathology was observed in the heart, liver, spleen, lung, or kidney of mice before and after injection of the $Cu_2O@SnO_2$ nanocatalyst. Meanwhile, the test results of ALT/AST/HCT/RBC also indicate that the $Cu_2O@SnO_2$ nanocatalyst has good biocompatibility (Fig. S5, ESI†). Inspired by the excellent *in vitro* ROS-releasing efficacy of the $Cu_2O@SnO_2$ nanocatalyst, 4T1-tumor-bearing mice were employed to evaluate the anti-tumor treatment

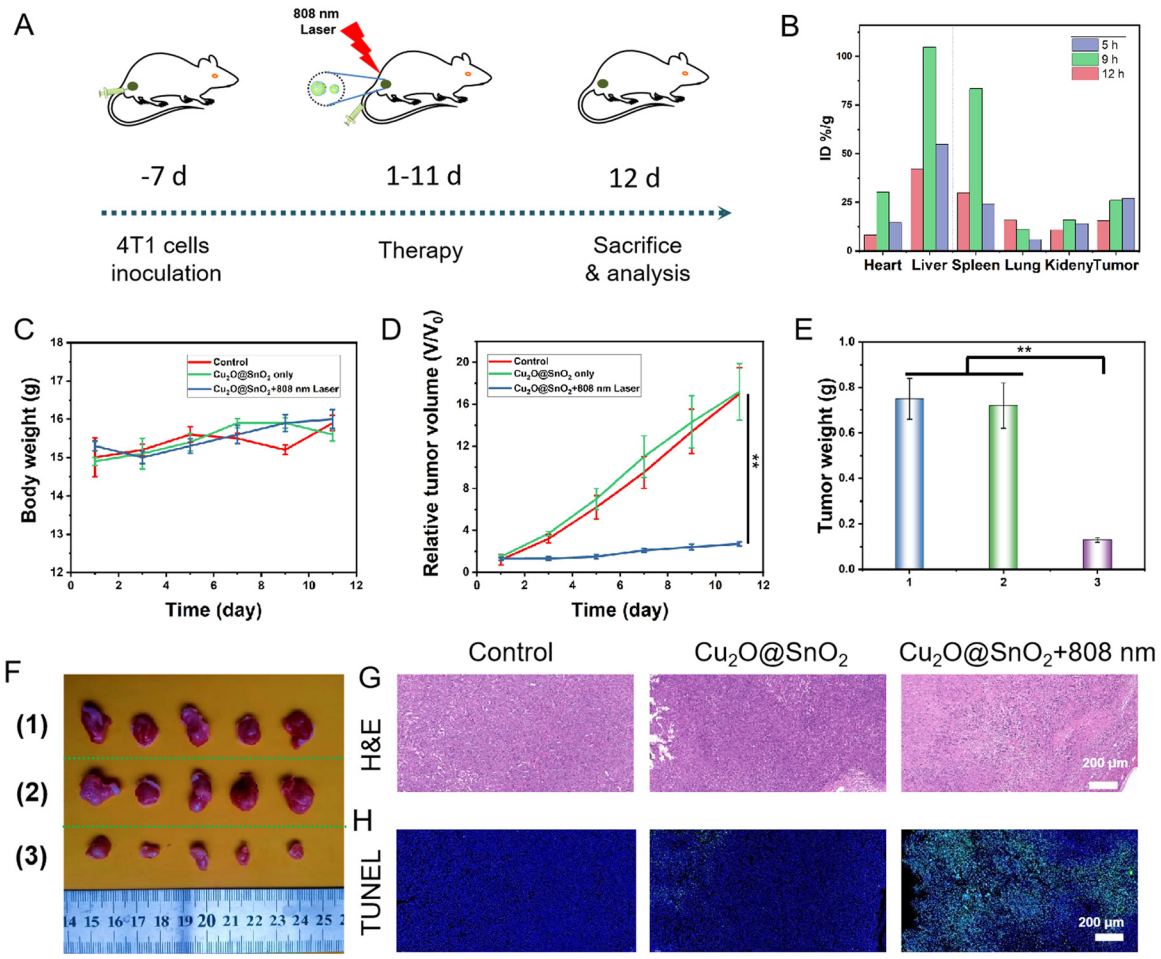

Fig. 4 808 nm light triggered ROS anti-tumor therapy *in vivo*. (A) Schematic illustration of the *in vivo* anti-tumor therapy based on the designed nanocatalyst. (B) Pharmacokinetic distribution of the $Cu_2O@SnO_2$ nanocatalyst. (C) Weight changes of the three groups of mice. (D)–(F) Tumor volume, weight, and photographs of tumors from the different groups (1): Control; (2): $Cu_2O@SnO_2$; (3): $Cu_2O@SnO_2$ + 808 nm laser). (G) and (H) H&E staining and TUNEL staining of 4T1-tumor-bearing mice from the four groups. Data are presented as mean ± SD., $^{**}p < 0.01$, $n = 5$.

efficacy of the $Cu_2O@SnO_2$ nanocatalyst (Fig. 4A). The 4T1-tumor-bearing mice were divided into three groups: PBS (control), $Cu_2O@SnO_2$ alone, and $Cu_2O@SnO_2$ + 808 nm laser. First, the quantitative bio-distribution of the $Cu_2O@SnO_2$ nanocatalyst *in vivo* was investigated using inductively coupled plasma mass spectrometry (ICP-MS). The uptaken $Cu_2O@SnO_2$ nanocatalyst mainly accumulated in the liver and tumor (Fig. 4B). Next, the body weight of the three groups remained stable after treatment, indicating the outstanding biocompatibility of the $Cu_2O@SnO_2$ nanocatalyst (Fig. 4C). Compared with the tumor growth observed in the control or only $Cu_2O@SnO_2$ nanocatalyst groups, the volume of tumors was effectively suppressed after treatment with the $Cu_2O@SnO_2$ nanocatalyst plus 808 nm laser (Fig. 4D–F), demonstrating high anti-tumor efficacy. We further studied the long-term survival of different treatment groups in the 4T1 mouse model (Fig. S6, ESI†) and found that the $Cu_2O@SnO_2$ nanocatalyst plus 808 nm laser irradiation group can significantly enhance the survival rate of the mice. Additionally, H&E and terminal deoxynucleotidyl transferase UTP nick end labeling (TUNEL) staining were used to evaluate the necrosis and apoptosis of 4T1 tumor cells (Fig. 4G–H). Obvious necrosis and apoptosis were observed in the group treated with the $Cu_2O@SnO_2$ nanocatalyst plus 808 nm laser irradiation. However, no apoptosis or necrosis were observed in tumor cells in the control and only $Cu_2O@SnO_2$ nanocatalyst treatment groups. We stained tumor sections with dihydroethidium (DHE) after different treatments to verify the production of ROS. As shown in Fig. S7A (ESI†), under the treatment of the $Cu_2O@SnO_2$ nanocatalyst plus 808 nm laser, an obvious green fluorescence signal can be seen by confocal image collection, verifying the therapeutic ability of the $Cu_2O@SnO_2$ nanocatalyst against tumors. Subsequently, the GSH levels in tumor tissues were assessed in different treatment groups. Compared with the other groups, the content of GSH in the $Cu_2O@SnO_2$ nanocatalyst + 808 nm laser group significantly decreased (Fig. S7B, ESI†). These results demonstrated that the $Cu_2O@SnO_2$ nanocatalyst had an efficient and sustained GSH consumption function and showed great application potential in ROS-based therapy. These results successfully indicated the superior therapeutic efficacy of the $Cu_2O@SnO_2$ nanocatalyst after 808 nm laser irradiation. The $Cu_2O@SnO_2$ nanocatalyst has become an ideal candidate for photocatalytic memory therapy due to its efficient storage and controllable release of photogenerated carriers, enhanced interface charge separation by its heterostructure, and the improved chemical stability of SnO_2. This material can continuously produce active oxygen in the dark, providing new strategies for deep tumor treatment and long-term environmental purification.

Conclusions

In summary, a novel $Cu_2O@SnO_2$ nanocatalyst has been successfully designed to continuously regulate oxidative stress in a tumor microenvironment through effective light energy storage and transformation. The $Cu_2O@SnO_2$ nanocatalyst can absorb and store light energy, release ROS and degrade GSH under 808 nm light irradiation. When the laser is turned off, the trapped electrons are released from SnO_2, generating ROS and GSH degradation. Our work shows that the selection of a photocatalyst system with a photocatalytic ''memory'' effect after irradiation may have broad therapeutic potential for deep-tissue malignant tumors.

Conflicts of interest

The authors declare no competing interests.

Data availability

The authors confirm that the data supporting the findings of this study are available within the article and/or its ESI.†

Acknowledgements

This work was supported by Youth Science Fund Project of the National Natural Science Foundation of China (NSFC) 12404204, Youth Foundation Project of the Natural Science Foundation of Hunan Province 2024JJ6116, Natural Science Foundation Project of Changsha City kq2402049 and the Science and Technology Program of Hunan Province, China (Grant No. 2019TP1014).

References

1 Z. X. Yang, C. H. Chen, B. Li, Y. F. Zheng, X. M. Liu, J. Shen, Y. Zhang and S. L. Wu, A cor-shell 2D-MoS_2@MOF heterostructure for rapid therapy of bacteria-infected wounds by enhanced photocatalysis, *Chem. Eng. J.*, 2023, **451**, 139127.
2 S. W. Guan, Z. H. Hou, J. Tan, X. M. Zhang, J. Y. Liu, H. H. Du, H. Q. Zhu, Y. Q. Qiao, Z. X. Liu and X. Y. Liu, Straddle-type heterostructure films endow titanium implant with NIR photocatalysis property for rapid sterilization, *Appl. Catal., B*, 2023, **334**, 122826.
3 Z. F. Huang, J. J. Song, L. Pan, X. W. Zhang, L. Wang and J. J. Zou, Tungsten Oxides for Photocatalysis, Electrochemistry, and Phototherapy, *Adv. Mater.*, 2015, **27**, 5309–5327.
4 S. Rawalekar and T. Mokari, Rational design of hybrid nanostructures for advanced photocatalysis, *Adv. Energy Mater.*, 2013, **3**, 12–27.
5 M. R. Hoffmann, S. T. Martin, W. Choi and D. W. Bahnemann, Environmental applications of semiconductor photocatalysis, *Chem. Rev.*, 1995, **95**, 69–96.
6 J. Liu, Y. Liu, N. Y. Liu, Y. Z. Han, X. Zhang, H. Huang, Y. Lifshitz, S. T. Lee, J. Zhong and Z. H. Kang, Metal-free efficient photocatalyst for stable visible water splitting via a two-electron pathway., *Science*, 2015, **347**, 970–974.
7 L. D. Li, J. Q. Yan, T. Wang, Z. J. Zhao, J. Zhang, J. Gong and N. J. Guan, Sub-10nm rutile titanium dioxide nanoparticles for efficient visible-light-driven photocatalytic hydrogen production, *Nat. Commun.*, 2015, **6**, 5881.

8 Y. Mi and Y. Weng, Band alignment and controllable electron migration between rutile and anatase TiO_2, *Sci. Rep.*, 2015, **5**, 11482.
9 L. Zhou, H. Zheng, Z. X. Liu, S. Q. Wang, Z. Liu, F. Chen, H. P. Zhang, J. Kong, F. T. Zhou and Q. Y. Zhang, Conductive Antibacterial Hemostatic Multifunctional Scaffolds Based on Ti_3C_2Tx MXene Nanosheets for Promoting Multidrug-resistant Bacteria-infected Wound Healing., *ACS Nano*, 2021, **15**, 2468–2480.
10 C. Zhang, Y. N. Gu, G. X. Teng, L. P. Wang, X. D. Jin, Z. W. Qiang and W. G. Ma, Fabrication of a Double-Shell Ag/AgCl/G-$ZnFe_2O_4$ Nanocube with Enhanced Light Absorption and Superior Photocatalytic Antibacterial Activity, *ACS Appl. Mater. Interfaces*, 2020, **12**, 29883–29898.
11 L. W. Wang, X. Zhang, X. Yu, F. E. Gao, Z. Y. Shen, X. L. Zhang, S. G. Ge, J. Liu, Z. J. Gu and C. Y. Chen, An All-organic Semiconductor C_3N_4/PDINH Heterostructure with Advanced Antibacterial Photocatalytic Therapy Activity, *Adv. Mater.*, 2019, **31**, 1901965.
12 J. C. Li, X. R. Yu, Y. Y. Jiang, S. S. He, Y. Zhang, Y. Luo and K. Y. Pu, Second Near-infrared Photothermal Semiconducting Polymer Nanoadjuvant for Enhanced Cancer Immunotherapy, *Adv. Healthcare Mater.*, 2021, **33**, 2003458.
13 J. S. Huang, J. G. Huang, P. H. Cheng, Y. Y. Jiang and K. Y. Pu, Near-infrared Chemiluminescent Reporters for in vivo Imaging of Reactive Oxygen and Nitrogen Species in Kidneys, *Adv. Funct. Mater.*, 2020, **30**, 2003628.
14 H. T. Bi, Y. L. Dai, P. P. Yang, J. T. Xu, D. Yang, S. L. Gai, F. He, B. Liu, C. N. Zhong, G. H. An and J. Lin, Glutathione Mediated Size-tunable UCNPs-Pt(IV)-$ZnFe_2O_4$ Nanocomposite for Multiple Bioimaging Guided Synergetic Therapy, *Small*, 2018, **14**, 1703809.
15 D. Wang, L. Zhu, J. F. Chen and L. M. Dai, Liquid Marbles Based on Magnetic Upconversion Nanoparticles as Magnetically and Optically Responsive Miniature Reactors for Photocatalysis and Photodynamic Therapy, *Angew. Chem., Int. Ed.*, 2016, **55**, 10795–10799.
16 Q. Li, Y. W. Li, P. G. Wu, R. C. Xie and J. K. Shang, Palladium oxide nanoparticles on nitrogen-doped titanium oxide: Accelerated photocatalytic disinfection and post-illumination catalytic ''memory'', *Adv. Mater.*, 2008, **20**, 3717–3723.
17 L. M. Liu, W. Y. Yang, Q. Li, S. A. Gao and J. K. Shang, Synthesis of Cu_2O nanospheres decorated with TiO_2 nanoislands, their enhanced photoactivity and stability under visible light illumination, and their post-illumination catalytic memory., *ACS Appl. Mater. Interfaces*, 2014, **6**, 5629–5639.
18 G. S. Hong, A. L. Antaris and H. J. Dai, Near-infrared Fluorophores for Biomedical Imaging, *Nat. Biomed. Eng.*, 2017, **1**, 0010.
19 G. S. Hong, S. Diao, J. L. Chang, A. L. Antaris, C. X. Chen, B. Zhang, S. Zhao, D. N. Atochin, P. L. Huang, K. I. Andreasson, C. J. Kuo and H. J. Dai, Through-skull Fluorescence Imaging of the Brain in a New Near-infrared Window, *Nat. Photonics*, 2014, **8**, 723–730.
20 J. Qi, C. Sun, A. Zebibula, H. Q. Zhang, R. T. K. Kwok, X. Y. Zhao, W. Xi, J. W. Y. Lam, J. Qian and B. Z. Tang, Real-time and High-resolution Bioimaging with Bright Aggregation-induced Emission Dots in Short-wave Infrared Region, *Adv. Mater.*, 2018, **30**, 1706856.
21 C. Y. Li, W. F. Li, H. H. Liu, Y. J. Zhang, G. C. Chen, Z. J. Li and Q. B. Wang, An Activatable NIR-II Nanoprobe for *in vivo* Early Real-time Diagnosis of Traumatic Brain Injury, *Angew. Chem., Int. Ed.*, 2020, **59**, 247–252.
22 R. Tian, H. L. Ma, S. J. Zhu, J. Lau, R. Ma, Y. J. Liu, L. Lin, S. Chandra, S. Wang, X. F. Zhu, H. Z. Deng, G. Niu, M. X. Zhang, A. L. Antaris, K. S. Hettie, B. Yang, Y. Y. Liang and X. Y. Chen, Multiplexed NIR-II Probes for Lymph Node-invaded Cancer Detection and Imaging-guided Surgery, *Adv. Mater.*, 2020, **32**, 1907365.
23 Y. Huang, J. L. Li, H. Feng, H. Du and Z. M. Deng, A Rapidly Synthesized, Ultra-Small Silver Nanocluster for Near-Infrared-II Imaging and Metabolic Studies, *Nano Lett.*, 2025, **25**, 854–860.
24 H. T. Bi, Y. L. Dai and P. P. Yang, Glutathione Mediated Size-tunable UCNPs-Pt(IV)-ZnFe2O4 Nanocomposite for Multiple Bioimaging Guided Synergetic Therapy, *Small*, 2018, **14**, 1703809.
25 D. Wang, L. Zhu and J. F. Chen, Liquid Marbles Based on Magnetic Upconversion Nanoparticles as Magnetically and Optically Responsive Miniature Reactors for Photocatalysis and Photodynamic Therapy, *Angew. Chem., Int. Ed.*, 2016, **55**, 10795–10799.
26 S. He, N. J. J. Johnson and V. A. N. Huu, Leveraging Spectral Matching between Photosensitizers and Upconversion Nanoparticles for 808 nm-activated Photodynamic Therapy, *Chem. Mater.*, 2018, **30**, 3991–4000.
27 A. N. Koo, K. H. Min, H. J. Lee, S. U. Lee, K. Kim, I. C. Kwon, S. H. Cho, S. Y. Jeong and S. C. Lee, Tumor Accumulation and Antitumor Efficacy of Docetaxel-loaded Core-shell-corona Micelles with Shell-specific Redox-responsive Cross-links, *Biomaterials*, 2012, **33**, 1489–1499.
28 L. Wang, Y. T. Xu, C. Liu, W. L. Si, W. J. Wang, Y. W. Zhang, L. P. Zhong, X. C. Dong and Y. X. Zhao, Copper-doped MOF-based nanocomposite for GSH depleted chemo/photothermal/chemodynamic combination therapy, *Chem. Eng. J.*, 2022, **438**, 135567.
29 B. Zhao, Y. S. Wang and X. X. Yao, Photocatalysis-mediated drug-free sustainable cancer therapy using nanocatalyst, *Nat. Commun.*, 2021, **12**, 1345.
30 L. M. Liu, W. Z. Sun, W. Y. Yang, Q. Li and J. Ku, Post-illumination activity of SnO_2 nanoparticle-decorated Cu_2O nanocubes by H_2O_2 production in dark from photocatalytic ''memory'', *Sci. Rep.*, 2016, **6**, 20878.
31 X. Y. Zhong, X. W. Wang and L. Cheng, GSH-depleted $PtCu_3$ Nanocages for Chemodynamic-enhanced Sonodynamic Cancer Therapy, *Adv. Funct. Mater.*, 2020, **30**, 1907954.

